Neurobiology of Disease 130 (2019) 104501

Contents lists available at ScienceDirect

Neurobiology of Disease

journal homepage: www.elsevier.com/locate/ynbdi

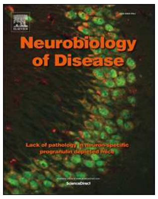

Diffusion tensor imaging identifies aspects of therapeutic estrogen receptor β ligand-induced remyelination in a mouse model of multiple sclerosis

Kelley C. Atkinson[a,1], Jeong Bin Lee[b,1], Jonathan P.C. Hasselmann[a], Sung Hoon Kim[c], Alyson Drew[b], Joselyn Soto[a], John A. Katzenellenbogen[c], Neil G. Harris[d], Andre Obenaus[b,e], Seema K. Tiwari-Woodruff[a,*]

[a] *Division of Biomedical Sciences, School of Medicine at UCR, Riverside, CA, USA*
[b] *Division of Physiology, School of Medicine at Loma Linda University, Loma Linda, CA, USA*
[c] *Department of Chemistry, University of Illinois at Urbana-Champaign, IL, USA*
[d] *Department of Neurosurgery, School of Medicine at UCLA, Los Angeles, CA, USA*
[e] *Department of Pediatrics, School of Medicine at UCI, Irvine, CA, USA*

ARTICLE INFO

Keywords:
Cuprizone diet
Demyelination
Neurodegeneration
Estrogen
Neuroprotection
Oligodendrocyte

ABSTRACT

Diffusion tensor imaging (DTI) has been shown to detect white matter degeneration in multiple sclerosis (MS), a neurodegenerative autoimmune disease that presents with diffuse demyelination of the central nervous system. However, the utility of DTI in evaluating therapeutic remyelination has not yet been well-established. Here, we assessed the ability of DTI to distinguish between remyelination and neuroprotection following estrogen receptor β ligand (Indazole chloride, IndCl) treatment, which has been previously shown to stimulate functional remyelination, in the cuprizone (CPZ) diet mouse model of MS. Adult C57BL/6 J male and female mice received a normal diet (control), demyelination-inducing CPZ diet (9wkDM), or CPZ diet followed by two weeks of a normal diet (*i.e.*, remyelination period) with either IndCl (RM + IndCl) or vehicle (RM + Veh) injections. We evaluated tissue microstructure of the corpus callosum utilizing *in vivo* and *ex vivo* DTI and immunohistochemistry (IHC) for validation. Compared to control mice, the 9wkDM group showed decreased fractional anisotropy (FA), increased radial diffusivity (RD), and no changes in axial diffusivity (AD) both *in vivo* and *ex vivo*. Meanwhile, RM + IndCl groups showed increased FA and decreased RD *ex vivo* compared to the RM + Veh group, in accordance with the evidence of remyelination by IHC. In conclusion, the DTI technology used in the present study can identify some changes in myelination and is a valuable translational tool for evaluating MS pathophysiology and therapeutic efficacy.

1. Introduction

Multiple sclerosis (MS) is an autoimmune, demyelinating, and neurodegenerative disease of the central nervous system (CNS) that affects about 2.3 million people worldwide (Browne et al., 2014) (Thompson et al., 2018). Due to widespread demyelination and axonal damage, MS patients exhibit a variety of symptoms, including problems with vision due to optic neuritis, motor deficits, and cognitive dysfunction (Thompson et al., 2018). The gold standard for MS diagnosis is magnetic resonance imaging (MRI). The criterion is based on longitudinal detection of lesions with abnormalities in T1 and T2 hyperintensities over time (McDonald et al., 2001). Although MS-related pathology and MRI change can be seen anywhere in the CNS, conventional MRI cannot differentiate lesions that are due to demyelination and/or axonal damage. Diffusion tensor imaging (DTI), however, has revolutionized clinical neuroimaging by allowing for the detection of demyelination and axonal pathology earlier and with greater specificity than conventional MRI (Song et al., 2003). DTI examines water diffusion within the white matter tissue (*i.e.*, the degree and direction of water diffusion along multiple axes) through tensor-model based

---

Abbreviations: DTI, diffusion tensor imaging; IndCl, Indazole chloride/Chloroindazole; MS, multiple sclerosis; DM, demyelination; RM, remyelination; CPZ, cuprizone; AD, axial diffusion; FA, fractional anisotropy; RD, radial diffusion; IHC, immunohistochemistry; ERβ, estrogen receptor beta; CC, corpus callosum

[*] Corresponding author at: Division of Biomedical Sciences, School of Medicine at the University of California Riverside, Rm 3140, Multidisciplinary Research Building, 900 University Ave, Riverside, CA 92521, USA.

E-mail addresses: seema.tiwari-woodruff@medsch.ucr.edu, seema-tiwari-woodruff@axonremyelination.org (S.K. Tiwari-Woodruff).

[1] Kelley C. Atkinson and Jeong Bin Lee are considered first co-authors.

https://doi.org/10.1016/j.nbd.2019.104501
Received 1 January 2019; Received in revised form 25 April 2019; Accepted 10 June 2019

reconstruction. This method provides valuable information regarding tissue microstructure, based on several metrics (Basser et al., 1994; Le Bihan et al., 2001; Mori and Zhang, 2006). Fractional anisotropy (FA) represents the asymmetry or directionality of water diffusion (FA = 1, anisotropic diffusion; FA = 0, isotropic diffusion), while mean diffusivity (MD) examines the average magnitude of water diffusion within a voxel. Other metrics include axial diffusivity (AD, λ_{II}), which reflects water diffusion along the axon and measures axon integrity, whereas radial diffusivity (RD, $\lambda_{\perp}$) reflects water diffusion perpendicular to axons, thereby measuring myelin integrity. With such metrics, DTI has been effectively used to quantify demyelination and axonal loss in MS patients (Elshafey et al., 2014; Hesseltine et al., 2006; Klawiter et al., 2011; Ontaneda et al., 2014).

Current MS drugs, including interferon β, glatiramer acetate, and fingolimod, are immunomodulatory and do not directly stimulate remyelination or confer neuroprotection (Lopez-Diego and Weiner, 2008; Thompson et al., 2018). Effective treatment options to initiate remyelination and prevent neurodegeneration are needed, as MS displays characteristics of a classical neurodegenerative disorder with damage to axons, synapses, and nerve cell bodies, along with rampant demyelination. The therapeutic efficacy of new MS treatments is usually tested in MS mouse models such as the experimental autoimmune encephalomyelitis (EAE) model, which incorporates key pathological components of MS (Baxter, 2007; Lucchinetti et al., 2000; Mangiardi et al., 2011). However, the chronic cuprizone diet (CPZ) mouse model has been shown to be better suited for studying the progressive stage of MS with demyelination, axon damage, astrogliosis, and microglial activation (Kipp et al., 2009; Lapato et al., 2017; Matsushima and Morell, 2001; Moore et al., 2014). Further, this model is advantageous when evaluating disease progression and therapies that target such degeneration given its consistent demyelination in structures such as the corpus callosum (CC) and superior cerebellar peduncles (Kipp et al., 2009; Matsushima and Morell, 2001). Cuprizone diet for 6 weeks is sufficient for substantial demyelination. However, this timepoint demonstrates some variability resulting from an extensive attempt to remyelinate the CNS, which starts early, even before cuprizone exposure terminates, confounding interpretation and drug-induced remyelination (Kipp et al., 2009; Matsushima and Morell, 2001). Thus, while cuprizone intoxication is inducing demyelination, oligodendrocyte progenitor cells (OPCs) are proliferating and differentiating to remyelinate axons during the 4–6 week cuprizone diet. By 9 weeks of cuprizone diet, there is near complete demyelination in the cortex, hippocampus, and CC and is an appropriate period to switch to normal diet to obtain clear axon remyelination for comparison with and without remyelinating drugs (Lapato et al., 2017; Moore et al., 2014).

Recently, estrogens have been evaluated for MS therapy due to their ability to stimulate myelination with neuroprotective benefits (Karim et al., 2018; Karim et al., 2019; Kumar et al., 2013; Moore et al., 2014; Offner et al., 2000; Sicotte et al., 2002; Tiwari-Woodruff et al., 2007). Due to estrogen receptor (ER) α-mediated feminization as well as increased risks of breast and uterine cancer, ERβ agonists have been considered more desirable therapeutic candidates (Lindberg et al., 2003). Ind-Cl is a unique, highly selective ERβ ligand that induces accelerated, functional remyelination in both EAE and CPZ mouse models of MS(Karim et al., 2019; Khalaj et al., 2016; Moore et al., 2014). IndCl not only improves clinical disease scores and rotarod performance but also stimulates remyelination and neuroprotection in the chronic CPZ model, with improvements in CC axon conduction (Karim et al., 2019; Moore et al., 2014).

While progress has been made in the development of novel therapies for MS, DTI's utility in evaluating therapeutic remyelination has not been well-established yet could prove critical given DTI's potential as a valuable tool for the research and development of novel remyelinating agents like IndCl. For longitudinal monitoring of MS pathophysiology and potential therapeutic efficacy, *in vivo* DTI can be utilized. In turn, *ex vivo* DTI provides improved imaging resolution for the detection of more subtle changes in white matter microstructure due to longer acquisition times and elimination of *in vivo* brain pulsations and movement artifacts.

The goal of this study was to utilize *in vivo* and *ex vivo* DTI in evaluating remyelination and neuroprotection following IndCl treatment in the CPZ diet-induced demyelination/remyelination model of MS. We hypothesized that DTI could adequately report CPZ-induced demyelination along with axonal damage as well as IndCl-induced therapeutic remyelination. This is the first study to evaluate the diagnostic potential of DTI with a remyelinating drug in an MS model. As such, it will serve as a first step towards longitudinal DTI assessment of white matter integrity in demyelinating MS models, which, combined with molecular and histological techniques, will streamline the screening process of therapeutic candidates and optimize the preclinical evaluation of their therapeutic potentials.

2. Materials and methods

2.1. Animals

This study followed the protocols established by the American Veterinary Medical Association in accordance with the National Institutes of Health (NIH) and were approved by the Institutional Animal Care and Use Committee (IACUC) at UCLA, Los Angeles and UCR, Riverside. Eight-week-old C57BL/6 J female and male mice were obtained from Jackson Laboratories and maintained in-house at the animal facility. Animals were allowed to acclimate for one full week at five per cage with standard light/dark cycles.

2.2. Treatment groups

Mice were assigned to two groups: normal diet (control; $n = 13$) and 0.2% cuprizone diet (CPZ) for nine weeks (9wkDM; $n = 41$) as previously described (Crawford et al., 2009; Lapato et al., 2017; Moore et al., 2014). Twenty-seven of the 9wkDM mice were then switched to two weeks of a normal diet and injected subcutaneously (s.c.) with either vehicle (RM + Veh; n = 13) or IndCl (RM + IndCl; $n = 14$) (Fig. 1A). Unless otherwise noted, all animals were included in all methods and subsequent analysis. IndCl (synthesized in the J.A.K. laboratories) was dissolved in 10% ethanol +90% (vol/vol) Miglyol 812 N (vehicle; Sasol) and administered at 5 mg/kg body weight in a volume of 0.1 ml/injection (De Angelis et al., 2005). Control groups received s.c. vehicle injections.

2.3. *In vivo* DTI imaging

2.3.1. MRI acquisition

Mice were anesthetized with 4% isofluorane in oxygen flowing at 0.6 L/min (control: $n = 7$; 9wkDM: n = 7; RM + Veh: $n = 5$; RM + IndCl: $n = 6$). Individual mice were transferred to a purpose-built cradle and secured using three-point immobilization of the head with two ear bars and a tooth bar. The mouse cradle was placed in the center of a 7 Tesla (T) spectrometer (Oxford Instr, Carteret, NJ, USA) driven by a Bruker console running Paravision 5.1 (Billerica, MA USA). Respiration was monitored remotely, and the temperature was homeothermically controlled by forced air (SA11 Instr, Inc., USA). The S116 Bruker gradients (400 mT/m) were used in combination with a birdcage transmit and an actively decoupled, receive-only, single-channel surface coil to acquire the data. Following a multi-slice, gradient-echo pilot scan to optimize positioning within the magnet, localized shimming was performed on the head to improve B0 homogeneity. A standard, 4-shot, spin echo, echo planar imaging sequence (38,000/23.3 ms repetition and echo time, respectively) was used to acquire diffusion-weighted images with directionally-encoded gradients applied along thirty different, even-spaced directions and with a b value of 1000 s/mm^2, using $\Delta = 10$ ms and $\delta = 4$ ms and one

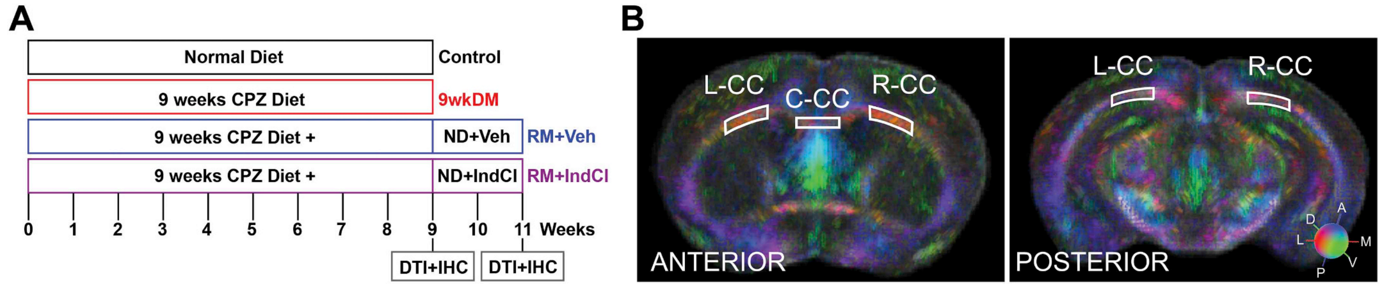

Fig. 1. Experimental design. (A) Eight-week-old male and female mice were fed either a normal diet (control; $n = 13$) or nine weeks of a 0.2% cuprizone (CPZ) diet (9wkDM; $n = 41$). After nine weeks, 27 9wkDM mice were switched to a normal diet for two weeks and received daily injections of an estrogen receptor β ligand IndCl (RM + IndCl; $n = 14$) or the vehicle (RM + Veh; n = 13). Brains were collected for immunohistochemistry (IHC) following *in vivo* diffusion tensor imaging (DTI), which was performed at week eleven for the aforementioned groups and week nine for the control and 9wkDM groups. Another cohort of mice underwent *ex vivo* DTI followed by IHC at weeks eleven and nine. (B) Regions were interrogated for fractional anisotropy values. Images at the antero-posterior level from Bregma 0.14/0.26 mm (anterior) and Bregma −2.92/3.08 mm (posterior) were utilized for tissue-level region analysis, chosen based on tract based spatial statistics (TBSS) data. *Ex vivo* DTI primary diffusion vectors modulated by group average fractional anisotropy (FA) for control and 9wkDM groups are shown (red = medial-lateral [X], green = dorsal-ventral [Y], blue = anterior-posterior [Z]). The following regions of interest (ROI) were analyzed: left CC (L-CC), center CC (C-CC), and right CC (R-CC). (For interpretation of the references to colour in this figure legend, the reader is referred to the web version of this article.)

additional image volume with a b value of 0 s/mm^2. All images were acquired with a 128-read and 128-phase-encoding matrix (X, Y direction respectively) within a 20mm^2 field-of-view and 20×14 1 mm contiguous, coronal slices, resulting in an in-plane resolution of 156×156 µm and a 1000 µm slice thickness. The number of averages (NEX) was 1.

2.3.2. Data analysis

Data were fitted for parametric images of FA, RD, and AD using FSL tools, (University of Oxford, UK). Spatial co-registration of the FA data to a single common mouse brain was accomplished using affine transformations and then applied to the other diffusivity indices.

2.4. Ex vivo DTI imaging

For *ex vivo* imaging, mice were deeply anesthetized by isoflurane (Piramal Healthcare) inhalation and perfused transcardially with 1 × PBS followed by 10% formalin (Thermo Fisher Scientific) with 10 mM Prohance (a Gadolinium, Gd agent) (control: $n = 6$; 9wkDM: $n = 8$; RM + Veh: n = 8; RM + IndCl: n = 8). While Gd is typically used to enhance T1 imaging, here, it was used to increase brain structural contrast during T2 weighted imaging. The perfused brains were preserved in PBS until they underwent DTI. High-resolution DTI imaging was acquired *ex vivo* using a 9.4 T Bruker Advance Imager with gradient amplitude of 720 mT/m (Experimental Imaging Centre, University of Calgary, Calgary, Canada; Paravision 5.1; Bruker Biospin, Billerica, MA). This higher field strength compared the 7 T used for *in vivo* imaging allows for improved SNR (Alexander et al., 2007). The data were collected using 128×128 matrix zero-filled to a final reconstruction of 256×256 matrix, with 15 mm × 15 mm field of view with 30×0.5 mm slices, 30 gradient directions, and 2 b-values (b = 0 and b = 3000 s/mm^2) with 5 b_0 images. Repetition time (TR)/echo time (TE) was 8000 ms/35.66 ms and number of averages (NEX) was 4. The larger b-value was used in the current experiments as it provides enhanced contrast particularly when using increased number of sampling directions (Tournier et al., 2013).

2.4.1. Data analysis

All data were fitted for parametric images of FA, RD, and AD using FSL tools, (University of Oxford, UK). Spatial co-registration of the FA data to a single common mouse brain was accomplished using affine transformations and then applied to the other diffusivity indices. Tract-based statistical analysis was conducted as before (Harris et al., 2016) with the exception that analysis was constrained to the CC, an area that has been shown to be significantly affected in this model (Crawford et al., 2009; Matsushima and Morell, 2001). All four experimental groups were entered into the general linear model for statistical inference of any effect between all groups, followed by posthoc testing with multiple contrasts for difference to control at the cluster-corrected level of $P < .05$ and z = 1.7 with a variance smoothing of 0.5 mm. A region-of-interest approach was also used by placing regions within the genu of the CC and the adjacent cingulum area (Fig. 1B). Regions were interrogated for mean diffusivity values. Images at the antero-posterior level from Bregma of 0.14/0.26 mm (anterior) and − 2.92/3.08 mm (posterior) were utilized for tissue-level region analysis, chosen based on TBSS data (Fig. 1B). In addition, the regional analysis was performed using DTI parametric maps generated in the DSI studio in native space (http://dsi-studio.labsolver.org). CC regions of interest (ROIs) were manually segmented by blinded experimenters.

2.5. Immunohistochemistry

In vivo DTI, *ex vivo* DTI, and non-DTI brain tissues were used for immunohistochemistry (IHC) analysis (control: $n = 6$; 9wkDM: $n = 8$; RM + Veh: n = 8; RM + IndCl: n = 8). For *ex vivo* DTI imaging, brains were rinsed with PBS after imaging to remove any remaining Prohance and were then cryoprotected in 30% sucrose (EMD Millipore, Darmstadt, Germany) for 48 h and embedded in gelatin for sectioning. *In vivo* DTI and non-DTI tissue were perfused transcardially with 1 × PBS followed by 10% formalin (Thermo Fisher Scientific) and were then cryoprotected in 30% sucrose (EMD Millipore, Darmstadt, Germany) for 48 h and embedded in gelatin for sectioning. Embedded brains were cut into 40 µm coronal sections using a HM525 NX cryostat (ThermoFisher Scientific). Sections were cut serially and stored in PBS with 1% sodium azide at 4 °C until stained. For IHC analysis, brain sections were permeabilized with 0.3% Triton X-100 in PBS and 15% normal goat serum (NGS). The following primary antibodies were used: chicken anti-myelin basic protein (MBP; AB9348, polyclonal, EMD Millipore, Darmstadt, Germany), mouse anti-neurofilament H non-phosphorylated (SMI-32; NE1023, monoclonal, EMD, Darmstadt, Germany), mouse anti-neurofilament M (NF-M; MAB1621, monoclonal, EMD Millipore, Darmstadt, Germany), chicken anti-glial fibrillary acidic protein (GFAP; AB5541, EMD Millipore, Darmstadt, Germany), myelin oligodendrocyte glycoprotein (MOG; MAB5680), and rabbit anti-Iba1 (Iba-1; 019–19,741, polyclonal, Wako). Secondary staining was performed using polyclonal fluorophore-conjugated antibodies: goat anti-chicken Alexa Fluor® 647 (Thermo Fisher Scientific), goat anti-mouse IgG Cy3 (EMD Millipore), goat anti-rabbit (Thermo Fisher Scientific), and goat anti-mouse IgG Cy3 (Life Technologies). Nuclei were counter stained with 4′, 6-Diamidino- 2-phenylindole (DAPI, 2 ng/

ml; Molecular Probes) for 10 min after incubation with secondary antibodies. Sections were mounted on glass slides, allowed to dry, and coverslipped with Fluoromount G mounting medium (ThermoFisher Scientific) for imaging.

2.6. Quantification and microscopy

Imaging was performed with an Olympus BX61 confocal microscope (Olympus America Inc., Center Valley, PA) and montages and z-stack projections were performed using CellSens and SlideBook6, respectively as previously described (Karim et al., 2019). The Olympus BX61 used spinning disk DSU-D4 with a slit width of 38 µm and slit spacing 400 µm. The pixel size of the Hamamatsu R2 was 6.45 µm pixels, Airy Disk was 0.28 µm with Nyquist sampling of 2.3. 10 ×, 20 ×, and 40 × objectives were used with step sizes 2.99 µm, 1.00 µm, and 0.740 µm with binning 1 and z stack between 20 and 30 µm. Counts and analysis of the center CC were performed blinded using ImageJ (NIH, Bethesda, MD). Stained sections from Bregma 0.14/0.26 mm (anterior sections) and − 2.92/3.08 mm (posterior sections) were chosen for 2-dimensional structural tensor analysis (Fig. 1). A plugin for ImageJ was utilized for characterization of the orientation and isotropic properties of SMI-32-stained axons and MBP-stained myelin in CC ROIs. Orientation J (Ori J; http://bigwww.epfl/ch/demo/orientation/; (Püspöki et al., 2016)), coherency values describing how coherently the appropriate stained pixels are orientated were obtained through quantitative orientation measurement by experimenters blinded to group assignment.

2.7. Statistical analysis

All statistics were performed using Prism 6 software (GraphPad Software, La Jolla, CA). DTI and immunohistochemistry data were analyzed by 2-tailed unpaired *t*-tests with Welch's correction comparing Control *vs.* 9wkDM and RM + Veh *vs.* RM + IndCl. Data are presented as mean ± SEM. Differences were considered significant at * $p < .05$, ** $p < .01$, *** $p < .001$, **** $p < .0001$.

3. Results

3.1. Attempted in vivo quantitative DTI measures do not adequately reflect demyelination and remyelination

The initial goal of this study was to evaluate brain demyelination and remyelination in a mouse model of MS by *in vivo* DTI. Sex- and age-matched C57Bl/6 J mice were placed on a 0.2% CPZ diet for nine weeks to induce chronic demyelination (9wkDM). After nine weeks on a CPZ diet, a subset of these mice were switched to a normal diet for two weeks to induce remyelination and, concurrently, injected with a known functionally remyelinating ERβ ligand IndCl (RM + IndCl) or the vehicle (RM + Veh) (Fig. 1A) (Moore et al., 2014). Because the CC is a major white matter tract that undergoes extensive demyelination during nine weeks on a CPZ diet, focused analysis of this commissural white matter tract of the left CC, center CC, and right CC was performed (Fig. 1B).

FA is a coefficient that reflects the magnitude and orientation of anisotropic water diffusion and is highly sensitive to white matter microstructural integrity (Feldman et al., 2010). Representative group average maps for FA in control and 9wkDM groups are shown in Fig. 2A. Changes in vector colour intensity in regions such as the CC and cingulum were observed qualitatively between the groups as indicated by white arrows. ROIs for left CC, center CC and right CC (Fig. 2B) were drawn manually and analyzed. Two-tailed, unpaired *t*-test with Welch's correction statistics were performed comparing control ($n = 5$) with 9wkDM ($n = 6$) and RM + Veh (n = 5) with RM + IndCl (n = 6). *In vivo* FA was decreased in the center and right CC of the 9wkDM group as compared to the control group ($p = .25$ left CC; $p = .02$ center CC; $p = .002$ right CC). However, no difference was observed between the RM + Veh and RM + IndCl groups ($p = .89$ left CC; $p = .82$ center CC; $p = .60$ right CC) (Fig. 2C). To further assess differences in demyelination and remyelination between the groups, RD and AD were measured *in vivo*. RD represents the diffusion perpendicular to the main axial direction and is known to be altered in response to experimental demyelination and dysmyelination (Alexander et al., 2007; Song et al., 2002; Song et al., 2005). RD analysis showed an increase in the left and right CC of the 9wkDM group compared to the control group ($p = .03$ left CC, $p = .69$ center CC, p = .03 right CC) (Fig. 2D). However, no difference in RD was observed between the RM + IndCl and RM + Veh groups ($p = .83$ left CC, $p = .52$ center CC, $p = .51$ right CC). AD is defined as the mean diffusion coefficient of water molecules diffusing parallel to the tract within the voxel (Song et al., 2003). Interestingly, *in vivo* AD in the CC did not differ between the control and 9wkDM groups or the RM + Veh and RM + IndCl groups (Fig. 2E) (control *vs.* 9wkDM: $p = .17$ left CC, p = .52 center CC, $p = .22$ right CC; RM + Veh *vs.* RM + IndCl: $p = .66$, $p = .24$, $p = .44$). Overall, *in vivo* DTI showed minimal differences in demyelination between control and 9wkDM and no differences between RM + Veh and RM + IndCl.

3.2. Chronically demyelinated CC shows decreased fractional anisotropy (FA) and mean diffusivity (MD) by tract-based spatial statistics (TBSS)

To enhance white matter resolution, *ex vivo* DTI was performed on a separate cohort of animals (control: n = 6; 9wkDM: $n = 8$; RM + Veh: n = 8; RM + IndCl: n = 8) (Fig. 3). Tract-based spatial statistics (TBSS) of the CC comparing the 9wkDM and control groups revealed that some CC regions in the 9wkDM group had lower FA (blue; Fig. 3A). This was also apparent in three dimensional (3D) reconstructions of the TBSS (Fig. 3B). FA revealed a decrease throughout the CC in the 9wkDM compared to the control group ($p = .0001$). However, no difference in FA TBSS was detected between the RM + Veh and RM + IndCl groups ($p = .53$) (Fig. 3C). TBSS-based MD analysis showed increased MD (red) in the 9wkDM group compared to the control group, indicating fewer barriers and more isotropic diffusion (Fig. 3D). 3D projection of these data illustrated that in the antero-lateral portion of the CC (red; Fig. 3E). Indeed, there was an overall increase in MD in the 9wkDM group compared to the control group throughout the CC ($p = .002$). However, no difference was observed between the RM + Veh and RM + IndCl groups ($p = .21$) (Fig. 3F). Overall, *ex vivo* DTI with TBSS analyses demonstrates changes in FA and MD in the chronically demyelinated CC.

3.3. Ex vivo DTI reveals corpus callosal changes in chronically demyelinated and IndCl-treated remyelinating groups

Since CPZ induces demyelination in distinct regions of the CC in a rostral to caudal fashion (Schmidt et al., 2012; Steelman et al., 2011), it is possible that remyelination events are differentially localized or below the detection threshold. Thus, assessment of local CC regions was performed by assigning ROIs (Fig. 4). Based on the results of Fig. 3, an anterior section (Bregma 0.14/0.26 mm) and a posterior section (Bregma −2.92/3.08 mm) were analyzed. The CC was analyzed by tracing *ex vivo* ROIs for left CC, center CC, and right CC for anterior sections and for left CC and right CC for posterior sections as shown in Fig. 1B and Supplementary Fig. S1. In anterior sections, the FA was reduced in the left, center, and right CC in the 9wkDM compared to the control group ($p < .0001$ left CC, $p = .02$ center CC, $p = .004$ right CC). In addition, the right CC FA was increased in the RM + IndCl group compared to the RM + Veh group ($p = .51$ left CC, $p = .30$ center CC, $p = .03$ right CC) (Fig. 4A). The MD in these sections was not different between the control and 9wkDM groups throughout the CC ($p = .96$ left CC, $p = .33$ center CC, $p = .98$ right CC); however, the MD in the left CC of the RM + IndCl group was reduced compared to the RM + Veh group ($p = .005$ left CC; $p = .09$ center CC, $p = .08$ right CC) (Fig. 4B). No difference in FA ($p = .05$ left CC, $p = .20$ right CC)

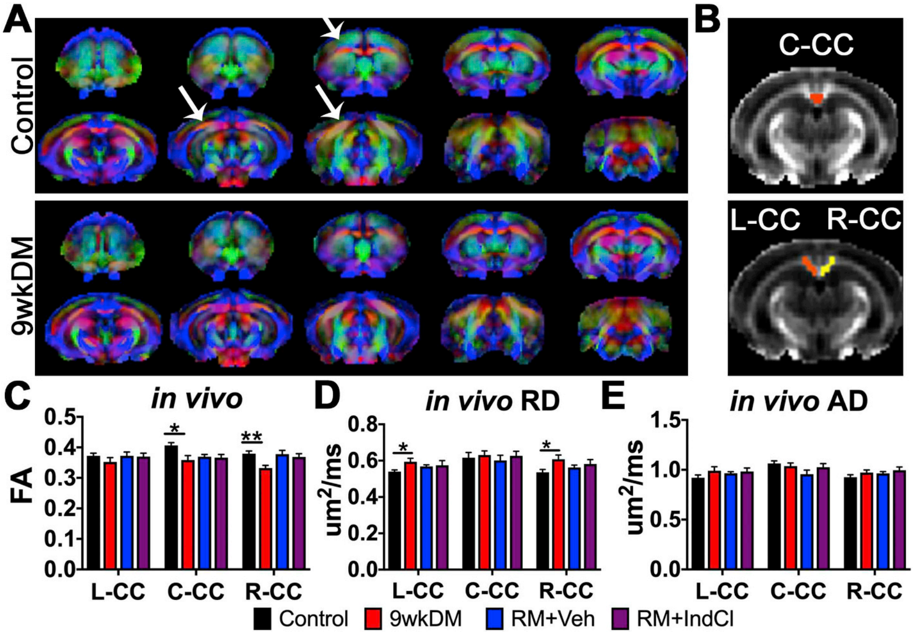

Fig. 2. *In vivo* DTI detects chronic CPZ-induced demyelination but not IndCl-induced remyelination. (A) *In vivo* primary diffusion vectors modulated by group average fractional anisotropy (FA) for control and 9wkDM groups (anterior to posterior sections from left to right, red = medial-lateral [X], green = dorsal-ventral [Y], blue = anterior-posterior [Z]). Diffusion data were warped to an anatomical template and used to calculate group averages. White arrows indicate areas that differ in FA between control and 9wkDM groups. (B) *In vivo* regions of interest for C-CC, L-CC, and R-CC were analyzed. (C) FA was decreased in the C– and R-CC of the 9wkDM compared to the control group. No differences in FA were detected between RM + Veh and RM + IndCl groups. (D) Radial diffusivity (RD) was increased in 9wkDM compared to the control groups in the L- and R-CC, while no differences in RD were observed between the RM + IndCl and RM + Veh groups. (E) No differences in axial diffusivity (AD) were observed between the control and 9wkDM groups, or between the RM + Veh and RM + IndCl groups. Control: *n* = 8; 9wkDM: *n* = 6; RM + Veh: *n* = 5; RM + IndCl: *n* = 6. Data are represented as mean ± SEM. $^*p < .05$, $^{**}p < .01$. (For interpretation of the references to colour in this figure legend, the reader is referred to the web version of this article.)

(Fig. 4C) or MD (Fig. 4D) was observed in the posterior section of 9wkDM and control groups ($p = .36$ left CC, $p = .13$ right CC). However, the left CC MD of the RM + IndCl group was decreased relative to the RM + Veh group ($p = .01$ left CC, $p = .22$ right CC). Because further imaging of posterior sections revealed fewer differences (Supplementary Fig. S1), we chose to focus the remainder of our study on the anterior sections for *ex vivo* DTI.

3.4. IndCl treatment during the remyelination phase does not affect radial diffusivity (RD)

To further delineate microstructural myelin changes indicated by the FA, we assessed RD (Fig. 5). *Ex vivo* TBSS for RD showed an increase in the 9wkDM group compared to the control group (red; Fig. 5A). Statistical summary of RD TBSS revealed an increase throughout the CC of the 9wkDM group compared to the control group (Fig. 5B). In contrast, RD quantification in the anterior section showed no difference in any region of the CC between the 9wkDM and control groups ($p = .37$ left CC, $p = .19$ center CC, $p = .43$ right CC) (Fig. 5C). However, there was a decrease in *ex vivo* RD in the RM + IndCl group in the left and right CC compared to the RM + Veh group ($p = .03$ left CC, $p = .39$ center CC, $p = .04$ right CC).

3.5. IndCl treatment during the remyelination phase potentiates remyelination

Based on the anterior and posterior *ex vivo* DTI results, IHC was performed to understand and compare DTI results to CPZ-induced

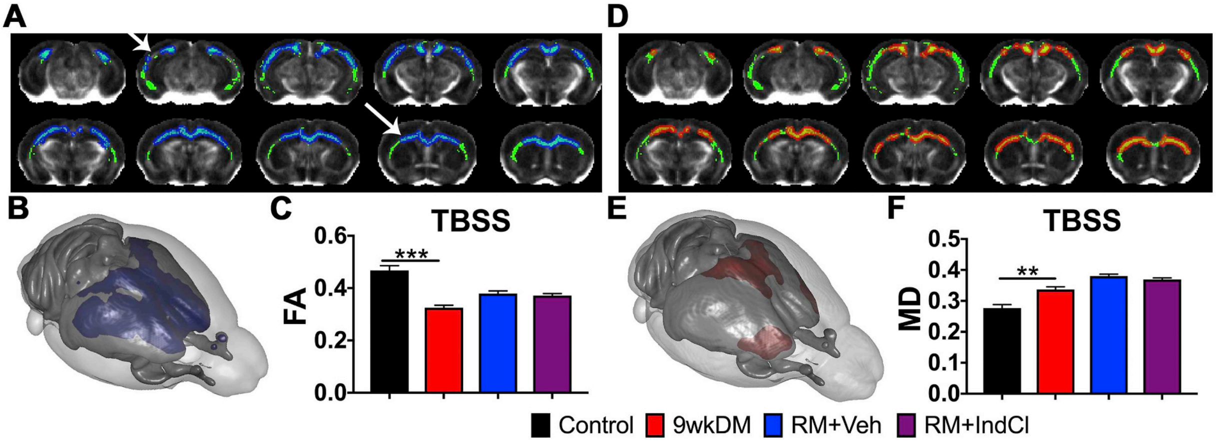

Fig. 3. Chronic CPZ diet results in reduced *ex vivo* fractional anisotropy (FA), with no detectable difference between vehicle and IndCl-treated remyelination (RM) groups. (A) Tract-based spatial statistics (TBSS) of the CC comparing the control and 9wkDM groups (green: white matter skeleton; blue: significant decrease). (B) Three-dimensional projection of a mouse brain (purple: a significant decrease in the 9wkDM group compared to the control group). (C) FA was decreased throughout the CC of the 9wkDM group compared to the control group. (D) Mean diffusivity (MD) TBSS ($\mu m^2/ms$) within CC comparing the 9wkDM and control groups (green: white matter skeleton; red: significant increase). (E) Three-dimensional projection of a mouse brain (red: a significant increase in the 9wkDM group compared to the control group). (F) MD was increased in the 9wkDM group compared to the control group. Control: *n* = 6; 9wkDM: *n* = 8; RM + Veh: n = 8; RM + IndCl: *n* = 8. Data are represented as mean ± SEM. $^{**}p < .01$, $^{***}p < .001$. (For interpretation of the references to colour in this figure legend, the reader is referred to the web version of this article.)

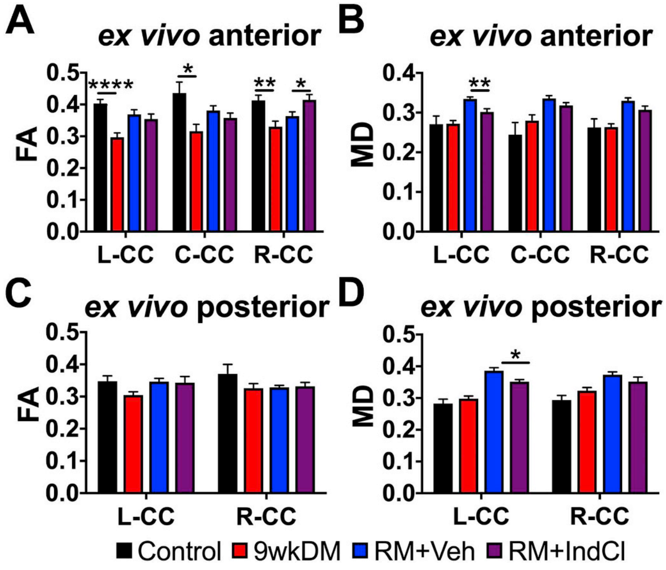

Fig. 4. *Ex vivo* DTI reveals differences in corpus callosal (CC) fractional anisotropy (FA) and mean diffusivity (MD) of chronic CPZ *versus* control groups, and IndCl *versus* vehicle-treated remyelination (RM) groups. (A) FA in anterior sections was decreased in the L-CC, C-CC, and R-CC of the 9wkDM group compared to the control group. In addition, FA was increased in the R-CC of the RM + IndCl group compared to the RM + Veh group. (B) MD did not differ between the control and 9wkDM groups throughout the CC but was decreased in the L-CC of the RM + IndCl group compared to the RM + Veh group. (C) No differences in FA were detected in the posterior CC of the 9wkDM group compared to the control group, or between the RM + Veh and RM + IndCl groups. (D) No differences were observed in the MD in posterior CC between the control and 9wkDM groups. MD was decreased in the L-CC of the RM + IndCl group compared to the RM + Veh group. Control: n = 6; 9wkDM: n = 8; RM + Veh: n = 8; RM + IndCl: n = 8. Data are represented as mean ± SEM. *p < .05, **p < .01, *****p* < .0001.

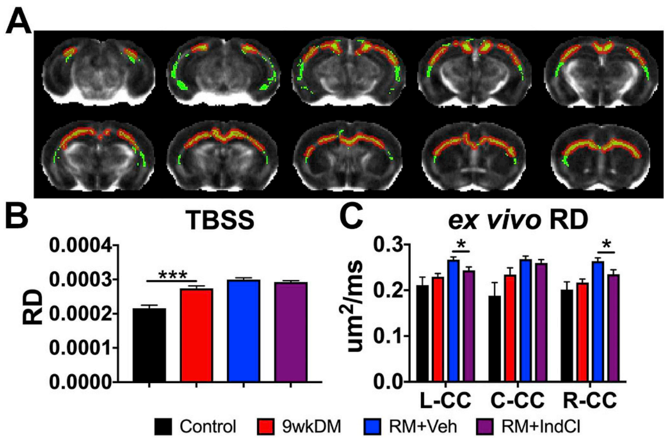

Fig. 5. IndCl-treated remyelination group decreases *ex vivo* corpus callosal (CC) radial diffusivity (RD) compared to the vehicle-treated group. (A) Tract-based spatial statistics (TBSS) of the CC comparing the control and 9wkDM groups for RD (green: white matter skeleton; red: significant increase). (B) RD was increased throughout the CC of the 9wkDM group compared to the control group. (C) *Ex vivo* RD in anterior sections had no differences detected between control and 9wkDM. RD was decreased in the RM + IndCl group compared to the RM + Veh group in the left and right CC. Control: n = 6; 9wkDM: n = 8; RM + Veh: n = 8; RM + IndCl: n = 8. Data are represented as mean ± SEM. *p < .05, ***p < .001. (For interpretation of the references to colour in this figure legend, the reader is referred to the web version of this article.)

demyelination followed by normal diet-induced remyelination effects. IHC was performed at the level of the dorsal hippocampus between the anterior and posterior DTI Bregmas (Fig. 6). To visualize changes in myelin, montages displaying myelin basic protein (MBP; green) and DAPI (blue) were imaged with staining intensity analyzed. MBP intensity was decreased in the 9wkDM group compared to the control group, with a dramatic increase in MBP expression in the RM + IndCl group as compared to the RM + Veh group (Fig. 6A, B). The center CC of the 9wkDM group showed a significant decrease in MBP intensity as compared to the control group (control *vs.* 9wkDM: *p* < .0001, Fig. 6C). There was, however, a significant increase in MBP intensity in the RM + IndCl group compared to the RM + Veh group (RM + Veh *vs.* RM + IndCl p < .0001, Fig. 6C). Similar changes were observed when the levels of another myelin protein, myelin oligodendrocyte glycoprotein (MOG) were measured (Supplementary Fig. S2). To further delineate changes in myelin organization, MBP coherency was quantified in the CC of anterior brain sections (Fig. 6D). There was an increase in MBP coherency (more coherently organized myelin) throughout the CC of the 9wkDM group compared to the control group (control *vs* 9wkDM: *p* = .0004 left CC, *p* = .001 center CC, p < .0001 right CC). In addition, an increase in coherency was observed in the RM + IndCl group in the left CC compared to the RM + Veh group (RM + Veh *vs* RM + IndCl: p = .04 left CC, *p* = .17 center CC, *p* = .14 right CC). Overall, while IndCl treatment increased myelination by IHC analysis (similar to published results (Moore et al., 2014)), DTI analysis demonstrated mixed results.

3.6. IndCl treatment during the remyelination phase minimally affects AD

Next, we assessed axonal integrity with AD (Fig. 7). *Ex vivo* TBSS assessed in the CC showed qualitative increases in AD between the 9wkDM and control groups (the red representing regions; Fig. 7A). Quantification of images across the CC showed an increase in AD TBSS in the 9wkDM group compared to the control group (p = .03) (Fig. 7B). However, there was no difference between the RM + Veh and RM + IndCl groups (*p* = .20). In contrast to the AD TBSS data, *ex vivo* analysis in the anterior sections displayed no significant differences between the 9wkDM and control groups (*p* = .27 left CC, *p* = .76 center CC, *p* = .41 right CC). There was an overall increase in *ex vivo* AD in the remyelinating groups. However, there was a decrease in AD in the RM + IndCl group compared to the RM + Veh group in the left and center CC (*p* = .003 left CC, p = .04 center CC, *p* = .51 right CC) (Fig. 7C).

3.7. IndCl treatment during the remyelination phase decreases NF-M+ intensity

Changes in AD are associated with axonal damage and loss. To assess whether the few changes in AD correlated with pathology, brain sections were immunostained for SMI-32. An increase in non-phosphorylated neurofilament reactivity is seen during demyelination as myelin is stripped, exposing denuded axons. SMI-32 intensity was quantified in the center CC as indicated on a coronal brain section montage immunostained with SMI-32 and DAPI (Fig. 8A). Representative 20× images for SMI-32 in the center CC are displayed in Fig. 8B. SMI-32 analysis showed increased SMI-32 expression in the 9wkDM group compared to the control group (*p* < .003) (Fig. 8C). In addition, the RM + IndCl group showed decreased SMI-32 expression compared to the RM + Veh group (*p* < .03) (Fig. 8C). Changes in axon pathology with demyelination and remyelination were also confirmed by neurofilament M (NF-M) intensity analysis, an additional marker for axon damage (Supplementary Fig. S3).

Astrogliosis (glial fibrillary acidic protein; GFAP) and microglial activation (Iba-1) immunostaining were also performed to assess the extent of inflammation and glia activation. Similar to previous results (Moore et al., 2014), there was an increase in GFAP and Iba-1 immunoreactivity in the CC of the 9wkDM group compared to the control group (Supplementary Fig. S4). Remyelination did not modify GFAP and Iba-1 levels, and these were similar to the 9wkDM group levels.

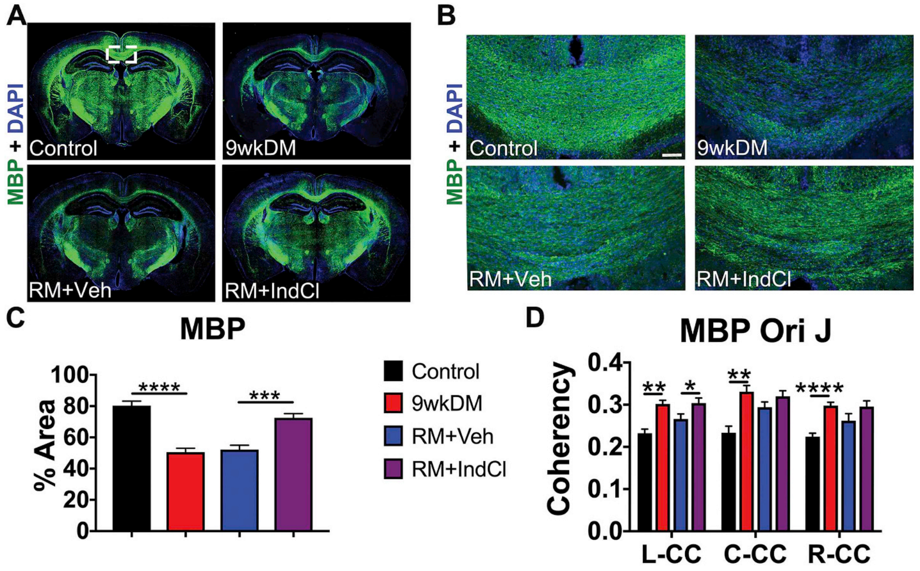

Fig. 6. IndCl-treated remyelination group increases myelination. (A) 10× montages displaying coronal sections of myelin basic protein (MBP; green) + 4′,6-diamidino-2-phenylindole (DAPI; blue). Representative montage of 9wkDM brain section shows a decrease in MBP staining intensity as compared to the control group. Whereas, RM + IndCl brain section shows an increase in staining intensity as compared to RM + Veh brain section. (B—C) Representative 10× images from the center CC from different groups immunostained with MBP show a similar result as in (A) and were used to quantify MBP intensity (scale bar = 50 μm) shown in (C). (D) Analysis of MBP Orientation J (Ori J) in the L-, C-, and R-CC revealed an increase in the anterior sections of the 9wkDM group compared to the control group in the entire CC. However, the RM + IndCl group had an increase in MBP Ori J coherency compared to the RM + Veh group only in the left CC. Control: n = 6; 9wkDM: n = 8; RM + Veh: n = 8; RM + IndCl: n = 8. Data are represented as mean ± SEM. *p < .05, **p < .01, ****p < .0001. (For interpretation of the references to colour in this figure legend, the reader is referred to the web version of this article.)

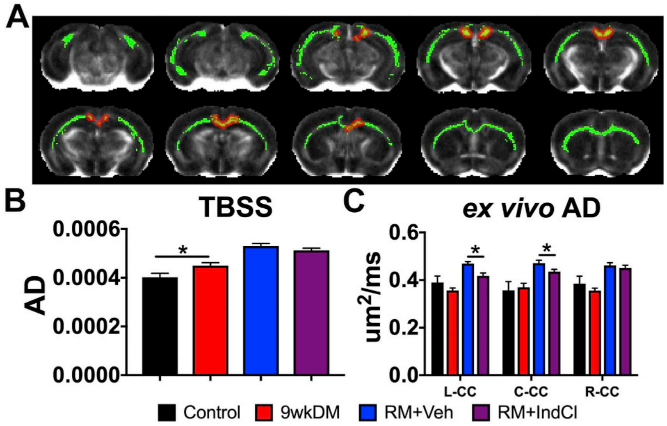

Fig. 7. IndCl-treated remyelination group decreases *ex vivo* axial diffusivity (AD). (A) Tract-based spatial statistics (TBSS) of the CC comparing the control and 9wkDM groups for AD (green: white matter skeleton; red: significant increase). (B) AD was increased throughout the CC of the 9wkDM group compared to the control group. (C*) Ex vivo* AD in anterior sections showed no difference between the control group and 9wkDM group. AD was decreased in the RM + IndCl group compared to the RM + Veh group. Control: n = 6; 9wkDM: n = 8; RM + Veh: n = 8; RM + IndCl: n = 8. Data are represented as mean ± SEM. **p* < .05. (For interpretation of the references to colour in this figure legend, the reader is referred to the web version of this article.)

In summary, Table 1 summarizes the DTI and IHC results. Overall, aspects of DTI were representative of demyelination and remyelination pathology; however, DTI may not purely report all aspects of the histologically observed pathology.

4. Discussion

Mouse models are often used to model human white matter disease; however, rodents possess significantly less white matter than humans, so assessing disease progression in rodents using MR imaging can be difficult in the context of myelination (Zhang and Sejnowski, 2000). Out of the various MS mouse models, the CPZ model provides reliable and reproducible white matter pathology (Mangiardi et al., 2011; Matsushima and Morell, 2001; Praet et al., 2014). The reproducibility of the CPZ model makes it well suited for studying mechanisms of demyelination and remyelination in the brain (Song et al., 2005; Xie et al., 2010; Yano et al., 2017), and for testing therapeutic treatments focused on improving axonal health and myelination.

In the present study, we included groups of mice that underwent CPZ-diet-induced chronic demyelination, followed by remyelination (initiated by switching to a normal diet) in the absence or presence of a known functionally remyelinating drug, IndCl. IndCl is a small, potent ERβ agonist with a 100:1 affinity for ERβ over ERα (De Angelis et al., 2005). IndCl has been previously shown to stimulate functional remyelination and neuroprotection by elevating neurotrophic factors and promoting oligodendrocyte survival and myelination through the PI3K/Akt/mTOR pathway (Moore et al., 2014; Saijo et al., 2011). Furthermore, IndCl decreases pro-inflammatory IFNγ levels while enhancing chemokine CXCL1 levels, which can also potentially indirectly increase myelination (Karim et al., 2018; Karim et al., 2019).

The control, demyelinating (9wkCPZ) and remyelinating groups (9wkCPZ + 2wkND with vehicle or IndCl) were assessed by *in vivo* DTI, *ex vivo* DTI, and IHC to monitor changes in axon and myelin pathology (Karim et al., 2018; Moore et al., 2014). Here, for the first time, using DTI image analysis as an outcome, we were able to discriminate drug-induced remyelination changes.

Past published studies have shown conflicting data with *in vivo* DTI during demyelination. An increase in RD and a decrease in FA was observed in one study using 4wk CPZ diet (Yano et al., 2017), whereas a decrease in FA and no apparent change in RD was observed in another study using 6wk CPZ diet (Zhang et al., 2012). In our present study, *in vivo* DTI study showed a significant reduction in callosal FA during CPZ demyelination with no change in RD, which is in congruence with Zhang et al. (Zhang et al., 2012). However, in our hands, *in vivo* DTI analysis failed to detect white matter microstructural alteration following normal diet-induced remyelination in the presence of IndCl treatment. No difference in FA or RD between RM + Veh and RM + IndCl was observed. This lack of difference could be due to incomplete remyelination after chronic CPZ diet, producing thinner myelin that evaded DTI changes (Duncan et al., 2017; Moore et al., 2014).

Since changes were apparent with *in vivo* DTI between control and 9wkDM groups, but not between the RM + Veh and RM + IndCl groups, *ex vivo* DTI was initiated to further assess demyelination and remyelination differences in an additional experiment. Our *ex vivo* TBSS data detected similar decreases to *in vivo* FA in the CC, as well as significant increases in MD in the 9wkDM group compared to the control

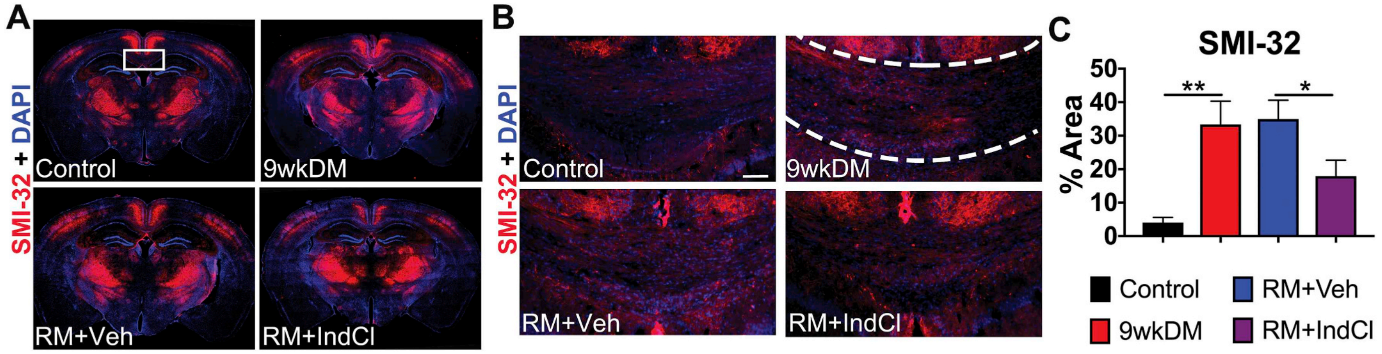

Fig. 8. IndCl-treated remyelination group decreases non-phosphorylated neurofilament (SMI-32+) expression. (A) 10× montages displaying SMI-32 (red), a marker for axon damage, + 4′,6-diamidino-2-phenylindole (DAPI; blue). The box represents 40× region where axon damage was imaged and analyzed in theC-CC. (B) 10× images for SMI-32 (red) + DAPI (blue). Scale bar = 50 μm. (C) The 9wkDM group has more SMI-32 expression compared to the control group in the center CC. In addition, the RM + IndCl group had decreased SMI-32 expression compared to the RM + Veh group. Control: n = 6; 9wkDM: n = 8; RM + Veh: n = 8; RM + IndCl: n = 8. Data are represented as mean ± SEM. *p < .05. (For interpretation of the references to colour in this figure legend, the reader is referred to the web version of this article.)

Table 1
Summary of results.

Variables	9wkDM *vs* normal									RM + IndCl *vs* RM + Veh								
	FA			RD			AD			FA			RD			AD		
	L	C	R	L	C	R	L	C	R	L	C	R	L	C	R	L	C	R
MRI																		
In vivo	–	↓	↓	↑	–	↑	–	–	–	–	–	–	–	–	–	–	–	–
Ex vivo	↓	↓	↓	–	–	–	–	–	–	–	–	↑	↓	–	↓	↓	↓	–
TBSS	↓			↑			↑			–			–			–		
IHC				MBP					SMI-32				MBP					SMI-32
				↓					↑				↑					↓

Note. 2-Tailed unpaired t-tests with Welch's correction. ↑ = significant increase, ↓ = significant decrease, – = no significant changes.

group. However, no significant changes in RD were observed even with *ex vivo* DTI. Previous studies exhibited that the rostral CC is less susceptible to pathological changes in chronic CPZ compared to the middle and caudal CC, which is why we analyzed the caudal CC (anterior Bregma) by IHC (Steelman et al., 2011; Wu et al., 2008; Xie et al., 2010). Our 9wkDM group showed demyelination, axon damage, astrogliosis, and microglial activation similar to previous studies (Varga et al., 2018). In addition, we observed a significant increase in coherency in MBP, indicating that MBP stained myelin was more coherently organized. Such results may reflect the altered organization of myelin due to the initial loss of myelin in the chronic demyelinated white matter. However, we saw no significant changes in SMI-32 coherency, which we interpret as surviving axons maintaining a similar orientation following demyelination.

Examination of specific CC regions in the remyelinating groups chosen based on *ex vivo* DTI TBSS data identified significant changes in FA and MD following RM + IndCl treatment as compared to RM + Veh alone. Such results signify not only that remyelination by IndCl was effective in altering white matter microstructure following experimental MS, but that only *ex vivo* data specific to the anterior regions of CC could detect these remyelination effects. Similar to previous results (Karim et al., 2019; Moore et al., 2014), the RM + IndCl group increased myelination and alleviated axon damage.

In essence, our study is one of the first to use DTI as a biomarker to evaluate CPZ-induced demyelination and remyelination with IndCl, an effective preclinical drug candidate. In the present *ex vivo* study, IndCl-treated mice showed a significant increase in FA compared to vehicle-treated mice. This result is expected due to increased anisotropy within the white matter voxels due to IndCl treatment-related stimulation of both remyelination and neuroprotection. These results also are in congruence with the significant decrease in RD observed *ex vivo* between the RM + IndCl and RM + Veh groups. However, the significant decrease in AD in the RM + IndCl group compared to the RM + Veh group was unexpected, because, as observed by IHC, IndCl decreased axon damage. However, it is important to note that DTI metrics do not match a single, specific physiological component. In fact, changes in axonal diameter, myelin distribution, axonal organization, intracellular compartments, and extracellular space can all contribute to changes in AD and overall DTI results (Thiessen et al., 2013; Yano et al., 2017; Zhang et al., 2012). Chronic demyelination changes are visible by *in vivo* and *ex vivo* DTI, but remyelination (induced with 3 week of normal diet) in the absence or presence of IndCl treatment produces thinner myelin around axons (Moore et al., 2014) as compared to myelinated axons in control mice. Thin myelin sheaths in the adult CNS is recognized as a marker of remyelination (shadow plaques in MS tissue (Popescu et al., 2013)) and the mechanism driving the incomplete recovery remains unknown (Duncan et al., 2017). More sophisticated DTI measures using multi-shell sequence, alternative microstructure models beyond diffusion tensor, and diffusion kurtosis-DK) may be useful in teasing apart aspects of demyelination and remyelination. A recent study demonstrated that DKI-derived metrics are indeed sensitive to 6 week CPZ induced demyelination and 3 week normal diet induced spontaneous remyelination of cortical areas (but not CC), thus highlighting the potential of kurtosis for the detection of grey matter alterations (Guglielmetti et al., 2016). Recently, a study performed to assess performance of DKI and DTI parameters in detecting microstructural changes and associated pathology in relapsing remitting MS (RRMS) provided some interesting results. DTI-derived diffusion parameters (FA, MD, and RD) detected abnormality in white matter regions with coherent fiber arrangement; however, the kurtosis parameters (mean kurtosis, MK, axial kurtosis, Ka, and radial kurtosis, Kr) were able to discern abnormalities in white matter regions with complex fibers (Li et al., 2018).

Diffusion scalars provide only a weighted mean of the pathology observed by IHC. For example, there is extensive demyelination, inflammation, reactive astrocyte accumulation and axon damage in the CC of 9wkDM mice as compared to controls that are not singularly reflected in either of the AD, RD, and FA values for both *in vivo* and *ex vivo* conditions. Furthermore, many factors can influence DTI outcomes and introduce variability between measurements (*in vivo vs. ex vivo*). *Ex vivo* images were acquired at a higher field strength at 9.4 T as compared to *in vivo* acquisition at only 7 T. The higher b-values used for *ex vivo* have been reported to be more sensitive towards slow-diffusing intra-axonal and myelin bound water and thus more sensitive to microstructural alterations within the white matter (Yoshiura et al., 2003). Several other reasons, such as changes in tissue temperature and increased membrane permeability due to cell death and brain fixation for the *ex vivo* samples, could contribute to variation between *in vivo* and *ex vivo* results (Shepherd et al., 2009). Finally, the diffusion time (Δ), which was adjusted to report optimal tissue diffusion in each condition, may play a role in producing the differences between *in vivo* and *ex vivo* data.

5. Conclusions

It is noteworthy that our FA values for the 9wkDM are similar to previously published studies that had chronic demyelination both *in vivo* and *ex vivo* (Chandran et al., 2012; Yano et al., 2017). In addition, our values for AD and RD for chronic CPZ *in vivo* and *ex vivo* are similar to previously published studies (Song et al., 2005; Thiessen et al., 2013; Zhang et al., 2012). While AD was not significant between control and 9wkDM, previous studies also did not reveal changes in AD after 12 weeks of chronic CPZ (Song et al., 2005). Interestingly, we did not see any significant changes in RD between 9wkDM and control. While 9 weeks of CPZ is known to induce demyelination, this lack of significant change in DTI could be due to the fact that *ex vivo* DTI data analyzed was more rostral CC where different parts of CC show differential demyelination patterns (Steelman et al., 2011; Xie et al., 2010).

While DTI is a valuable technique with great potential to be used as a biomarker, more advanced techniques may allow detection of more subtle physiological changes. IHC provides greater resolution compared to DTI, however, this technique cannot be used to measure patient's disease progression. Other imaging methods such as Generalized q-Sampling Imaging (GQI) and Diffusion Basis Spectrum Imaging (DBSI) may be utilized in conjunction with DTI in order to enhance pathology detection and therapeutic efficacy assessment (Yeh et al., 2010). Combining diffusion and kurtosis parameters could provide complementary information for revealing brain microstructural damage in animal models of MS and MS patients, where DKI parameters may be regarded as useful surrogate markers for reflecting pathological changes beyond demyelination and axon damage (Guglielmetti et al., 2016; Li et al., 2018). Emerging MS imaging studies are utilizing these combined methods, demonstrating the potential of advanced diffusion-weighted imaging methods in detecting and studying white matter microstructure in MS, both clinically and experimentally.

6. Study limitations

A limitation of the current study is that different cohorts were used for the *in vivo* and *ex vivo* studies. Although unlikely given the high reproducibility of the CPZ model, variations in the extent of demyelination and remyelination may have occurred to skew *in vivo* and *ex vivo* data. In addition, the contrast agent Gd was administered during brain fixation for the *ex vivo* group. Gd is effective in enhancing the T1 relaxation component of the overall MRI signal; however, its effect on DTI metrics is currently unclear. Two clinical studies have reported opposite effects on FA with Gd (Zolal et al., 2012). However, it is important to note that both studies report small non-significant changes in white matter FA, so the effects of contrast agent treatment on DTI is thought to be minimal. Future multi-shell DTI experiments should minimize many of these confounds as has been done in emerging human MS studies (Schneider et al., 2017).

Competing financial interests

The authors declare that they have no competing financial interests.

Declarations of interest

None.

Acknowledgments

This work was supported by National Institutes of Health Grants NIH R01 NS081141-01A1 to STW and NIH R01 DK015556 to JAK and by National Multiple Scelrosis Society grant NMSS RG 1853A3/2 to STW. We would like to thank Ms. Anna J. Khalaj for technical support.

Appendix A. Supplementary data

Supplementary data to this article can be found online at https://doi.org/10.1016/j.nbd.2019.104501.

References

Alexander, A.L., et al., 2007. Diffusion tensor imaging of the brain. Neurotherapeutics 4, 316–329.

Basser, P.J., et al., 1994. Estimation of the effective self-diffusion tensor from the NMR spin echo. J. Magn. Reson. B 103, 247–254.

Baxter, A.G., 2007. The origin and application of experimental autoimmune encephalomyelitis. Nat. Rev. Immunol. 7, 904–912.

Browne, P., et al., 2014. Atlas of multiple sclerosis 2013: a growing global problem with widespread inequity. Neurology 83, 1022–1024.

Chandran, P., et al., 2012. Magnetic resonance imaging and histological evidence for the blockade of cuprizone-induced demyelination in C57BL/6 mice. Neuroscience 202, 446–453.

Crawford, D.K., et al., 2009. Functional recovery of callosal axons following demyelination: a critical window. Neuroscience 164, 1407–1421.

De Angelis, M., et al., 2005. Indazole estrogens: highly selective ligands for the estrogen receptor β. J. Med. Chem. 48, 1132–1144.

Duncan, I.D., et al., 2017. Thin myelin sheaths as the hallmark of remyelination persist over time and preserve axon function. Proc. Natl. Acad. Sci. U. S. A. 114, E9685–E9691.

Elshafey, R., et al., 2014. Diffusion tensor imaging for characterizing white matter changes in multiple sclerosis. Egypt. J. Radiol. Nucl. Med. 45, 881–888.

Feldman, H.M., et al., 2010. Diffusion tensor imaging: a review for pediatric researchers and clinicians. J. Dev. Behav. Pediatr. 31, 346.

Guglielmetti, C., et al., 2016. Diffusion kurtosis imaging probes cortical alterations and white matter pathology following cuprizone induced demyelination and spontaneous remyelination. Neuroimage 125, 363–377.

Harris, N.G., et al., 2016. Bi-directional changes in fractional anisotropy after experiment TBI: disorganization and reorganization? Neuroimage 133, 129–143.

Hesseltine, S., et al., 2006. Diffusion tensor imaging in multiple sclerosis: assessment of regional differences in the axial plane within normal-appearing cervical spinal cord. Am. J. Neuroradiol. 27, 1189–1193.

Karim, H., et al., 2018. Increase in chemokine CXCL1 by ERbeta ligand treatment is a key mediator in promoting axon myelination. Proc. Natl. Acad. Sci. U. S. A. 115, 6291–6296.

Karim, H., et al., 2019. Analogues of ERbeta ligand chloroindazole exert immunomodulatory and remyelinating effects in a mouse model of multiple sclerosis. Sci. Rep. 9, 503.

Khalaj, A.J., et al., 2016. Nudging oligodendrocyte intrinsic signaling to remyelinate and repair: estrogen receptor ligand effects. J. Steroid Biochem. Mol. Biol. 160, 43–52.

Kipp, M., et al., 2009. The cuprizone animal model: new insights into an old story. Acta Neuropathol. 118, 723–736.

Klawiter, E.C., et al., 2011. Radial diffusivity predicts demyelination in ex vivo multiple sclerosis spinal cords. Neuroimage 55, 1454–1460.

Kumar, S., et al., 2013. Estrogen receptor β ligand therapy activates PI3K/Akt/mTOR signaling in oligodendrocytes and promotes remyelination in a mouse model of multiple sclerosis. Neurobiol. Dis. 0, 131–144.

Lapato, A.S., et al., 2017. Chronic demyelination-induced seizures. Neuroscience 346, 409–422.

Le Bihan, D., et al., 2001. Diffusion tensor imaging: concepts and applications. J. Magn. Reson. Imaging 13, 534–546.

Li, H.Q., et al., 2018. Evaluation of patients with relapsing-remitting multiple sclerosis using tract-based spatial statistics analysis: diffusion kurtosis imaging. BMC Neurol. 18, 108.

Lindberg, M.K., et al., 2003. Estrogen receptor (ER)-β reduces ERα-regulated gene transcription, supporting a “Ying Yang” relationship between ERα and ERβ in mice. Mol. Endocrinol. 17, 203–208.

Lopez-Diego, R.S., Weiner, H.L., 2008. Novel therapeutic strategies for multiple sclerosis—a multifaceted adversary. Nat. Rev. Drug Discov. 7, 909.

Lucchinetti, C., et al., 2000. Heterogeneity of multiple sclerosis lesions: implications for the pathogenesis of demyelination. Ann. Neurol. 47, 707–717.

Mangiardi, M., et al., 2011. An animal model of cortical and callosal pathology in multiple sclerosis. Brain Pathol. 21, 263–278.

Matsushima, G.K., Morell, P., 2001. The neurotoxicant, cuprizone, as a model to study demyelination and remyelination in the central nervous system. Brain Pathol. 11, 107–116.

McDonald, W.I., et al., 2001. Recommended diagnostic criteria for multiple sclerosis: guidelines from the international panel on the diagnosis of multiple sclerosis. Ann. Neurol. 50, 121–127.

Moore, S.M., et al., 2014. Multiple functional therapeutic effects of the estrogen receptor beta agonist indazole-Cl in a mouse model of multiple sclerosis. Proc. Natl. Acad. Sci. U. S. A. 111, 18061–18066.

Mori, S., Zhang, J., 2006. Principles of diffusion tensor imaging and its applications to basic neuroscience research. Neuron. 51, 527–539.

Offner, H., et al., 2000. Estrogen potentiates treatment with T-cell receptor protein of female mice with experimental encephalomyelitis. J. Clin. Invest. 105, 1465–1472.

Ontaneda, D., et al., 2014. Identifying the start of multiple sclerosis injury: a serial DTI study. J. Neuroimaging 24, 569–576.

Popescu, B.F., et al., 2013. Pathology of multiple sclerosis: where do we stand? Continuum (Minneap Minn.) 19, 901–921.

Praet, J., et al., 2014. Cellular and molecular neuropathology of the cuprizone mouse model: clinical relevance for multiple sclerosis. Neurosci. Biobehav. Rev. 47, 485–505.

Püspöki, Z., et al., 2016. Transforms and operators for directional bioimage analysis: a survey. In: Focus on Bio-Image Informatics. Springer, pp. 69–93.

Saijo, K., et al., 2011. An ADIOL-ERbeta-CtBP transrepression pathway negatively regulates microglia-mediated inflammation. Cell. 145, 584–595.

Schmidt, T., et al., 2012. Regional heterogeneity of cuprizone-induced demyelination: topographical aspects of the midline of the corpus callosum. J. Mol. Neurosci. 49, 80–88.

Schneider, T., et al., 2017. Sensitivity of multi-shell NODDI to multiple sclerosis white matter changes: a pilot study. Funct. Neurol. 32, 97–101.

Shepherd, T.M., et al., 2009. Aldehyde fixative solutions alter the water relaxation and diffusion properties of nervous tissue. Magn. Reson. Med. 62, 26–34.

Sicotte, N.L., et al., 2002. Treatment of multiple sclerosis with the pregnancy hormone estriol. Ann. Neurol. 52, 421–428.

Song, S.-K., et al., 2002. Dysmyelination revealed through MRI as increased radial (but unchanged axial) diffusion of water. Neuroimage 17, 1429–1436.

Song, S.-K., et al., 2003. Diffusion tensor imaging detects and differentiates axon and myelin degeneration in mouse optic nerve after retinal ischemia. Neuroimage 20, 1714–1722.

Song, S.K., et al., 2005. Demyelination increases radial diffusivity in corpus callosum of mouse brain. Neuroimage 26, 132–140.

Steelman, A.J., et al., 2011. Demyelination and remyelination in anatomically distinct regions of the corpus callosum following cuprizone intoxication. Neurosci. Res. 72, 32–42.

Thiessen, J.D., et al., 2013. Quantitative MRI and ultrastructural examination of the cuprizone mouse model of demyelination. NMR Biomed. 26, 1562–1581.

Thompson, A.J., et al., 2018. Multiple sclerosis. Lancet. 391, 1622–1636.

Tiwari-Woodruff, S., et al., 2007. Differential neuroprotective and antiinflammatory effects of estrogen receptor (ER)alpha and ERbeta ligand treatment. Proc. Natl. Acad. Sci. U. S. A. 104, 14813–14818.

Tournier, J.D., et al., 2013. Determination of the appropriate b value and number of gradient directions for high-angular-resolution diffusion-weighted imaging. NMR Biomed. 26, 1775–1786.

Varga, E., et al., 2018. Cuprizone administration alters the Iron metabolism in the mouse model of multiple sclerosis. Cell. Mol. Neurobiol. 1–17.

Wu, Q.Z., et al., 2008. MRI identification of the rostral-caudal pattern of pathology within the corpus callosum in the cuprizone mouse model. J. Magn. Reson. Imaging 27, 446–453.

Xie, M., et al., 2010. Rostrocaudal analysis of corpus callosum demyelination and axon damage across disease stages refines diffusion tensor imaging correlations with pathological features. J. Neuropathol. Exp. Neurol. 69, 704–716.

Yano, R., et al., 2017. Quantitative temporal changes in DTI values coupled with histological properties in cuprizone-induced demyelination and remyelination. Neurochem. Int. 119, 151–158.

Yeh, F.-C., et al., 2010. Generalized q-sampling imaging. IEEE Trans. Med. Imaging 29, 1626–1635.

Yoshiura, T., et al., 2003. High b value diffusion-weighted imaging is more sensitive to white matter degeneration in Alzheimer's disease. Neuroimage 20, 413–419.

Zhang, K., Sejnowski, T.J., 2000. A universal scaling law between gray matter and white matter of cerebral cortex. Proc. Natl. Acad. Sci. 97, 5621–5626.

Zhang, J., et al., 2012. In vivo and ex vivo diffusion tensor imaging of cuprizone-induced demyelination in the mouse corpus callosum. Magn. Reson. Med. 67, 750–759.

Zolal, A., et al., 2012. The effect of a gadolinium-based contrast agent on diffusion tensor imaging. Eur. J. Radiol. 81, 1877–1882.